Promotion of hydrocarbon selectivity in CO_2 hydrogenation by Ru component

Sung-Chul Lee[a], Jea-Hun Jang[a], Byung-Yong Lee[a], Jun-Sik Kim[c], Misook Kang[b], Sang-Bong Lee[c], Myung-Jae Choi[c], Suk-Jin Choung[a],*

[a] *College of Environmental Applied Chemistry, Kyung Hee University, Gyeonggi 449-701, South Korea*
[b] *Industrial Liaison Research Institute, Kyung Hee University, Gyeonggi 449-701, South Korea*
[c] *Chemical Technology Division, Korea Research Institute of Chemical Technology, Daejon 505-600, South Korea*

Abstract

We investigated catalytic behavior of iron in CO_2 hydrogenation with and without a ruthenium component. Calcined iron-based catalysts were reduced by H_2 and characterized by XRD, BET surface area and CO_2, CO and C_2H_4 temperature-programmed desorption (TPD), and tested for CO_2 hydrogenation. When Fe-K/γ-Al_2O_3 was used as a catalyst, CO_2 conversion was 36%, but when Fe-Ru-K/γ-Al_2O_3 was used, CO_2 conversion was 41%. The product selectivities for catalysts with and without the ruthenium component were also compared. Fe-K/γ-Al_2O_3 exhibited higher methane (16 mol%) and C_2–C_4 selectivity (39.6 mol%) than Fe-Ru-K/γ-Al_2O_3. The main products obtained with Fe-Ru-K/γ-Al_2O_3 were higher hydrocarbons such as $C_5{}^+$ hydrocarbons. For Fe-Ru-K/γ-Al_2O_3, the product distribution followed the Anderson–Schultz–Flory (ASF) distribution. However, in the case of Fe-Ru-K/γ-Al_2O_3, the hydrocarbon distribution deviates from the ideal ASF distribution. It is concluded that the readsorption rates of the primary hydrocarbon product increase exponentially with chain length in the ruthenium promoted catalytic system. The behavior of catalysts with and without the ruthenium will be explained by the CO_2-, CO- and C_2H_4- profiles. In this study, it was confirmed that ruthenium component promoted the readsorption ability of α-olefin, and then the chain length of hydrocarbon is higher. In addition, the microcrystalline wax produced in CO_2 hydrogenation was a high-crystalline and olefin-rich hydrocarbon.
© 2003 Elsevier B.V. All rights reserved.

Keywords: CO_2 hydrogenation; Fe-K/γ-Al_2O_3; Ruthenium component; ASF distribution

1. Introduction

The Fischers–Tropsch synthesis (FTS) has been extensively investigated since the discovery of methane production over nickel in 1902. In the past three decades, the hydrogenation of carbon monoxide (CO) was actively studied all over the world because it is an important step in the utilization of coal and natural gas as carbon sources. However, the hydrogenation of carbon dioxide (CO_2) received much less attention, partially due to unfavorable thermodynamic consideration. In recent years, global warming caused by CO_2 emissions had been recognized as an urgent problem. As a result, the chemical fixation of CO_2 has gained attention as one of the effective carbon dioxide utilizing technologies, and fixation by chemical methods are still a problem to be solved. The main problem in CO_2 hydrogenation is that its products are common and were low value materials [1]. However, CO_2 is available as an infinite carbon source. Therefore, producing valuable materials from CO_2 would promote the utilization of CO_2.

For the fixation of CO_2 emitted from industrial sources, various chemical processes for converting CO_2 into valuable chemical compounds have been attempted. One such process is to convert carbon dioxide into linear hydrocarbons; this reaction has already been thoroughly studied [2,3]. Many investigations have focused on direct synthesis of hydrocarbons from CO_2, on the catalytic synthesis of methanol from CO_2, and on the methanol to olefin (MTO) process [4,5]. Fujiwara et al. reported that the composite of Fe–Zn–Zr catalyst

* Corresponding author. Tel.: +82-31-201-2533;
fax: +82-31-202-1946.
E-mail address: sjchoung@khu.ac.kr (S.-J. Choung).

with H-ZSM-5 produced high-octane gasoline from carbon dioxide in good yield [6]. Dimethyl carbonate, which was widely used industrial applications as a monomer for polymers, solvents, or additive for fuel, was synthesized from carbon dioxide and methanol [7,8]. The reaction of CO_2 with methanol has been conducted in the presence of a basic catalyst and methyl iodide promoter [9]. Zhao et al. reported that direct synthesis of dimethyl carbonate at near supercritical conditions using nickel acetate [10]. It was reported that addition of a small amount of heavy 1-olefin into the supercritical phase FT reaction could significantly promote the chain growth and greatly enhance the selectivity of waxy products [11]. However, this phenomenon does not occur in the gas phase reaction. FT wax, having an advantage of high melting point, high hardness value, low viscosity, and being nitrogen-, sulfur-, and aromatic-free, is highly favorable. It could be used indirectly in many chemical fields such as cosmetics, packing materials, and adhesives. However, in the case of CO_2 hydrogenation, the formation of crystalline wax has not been reported.

Trovarelli et al. suggested that the hydrogenation of CO_2 to hydrocarbons proceeded through the formation of CO as intermediate [12]. According to other authors [13,14], CO_2 hydrogenation on metal catalysts occurred through a consecutive mechanism in which CO_2 was first converted to CO by the reverse water gas shift (RWGS) reaction, and then CO was hydrogenated to hydrocarbons. Therefore, the chain growth mechanism of hydrocarbon synthesis from carbon dioxide was similar to that of the FT reaction. Anderson, Schultz, and Flory suggested that the hydrocarbon chain was formed by insertion or addition of C_1 intermediates with constant growth probability. However, most iron-based catalyst deviated from the Anderson–Schultz–Flory (ASF) distribution. Gaube et al. [15] reported that the chain growth distribution was not uniform because of the different active sites due to the alkali promoter. Therefore, the product distribution of iron catalyst does not follow the ASF distribution. Iglesia et al. proposed [16,17] that all products formed by desorption from chain growth site were primary FT synthesis products. Secondary reactions altered FT synthesis selectivity by chemical transformations of these primary products. In many cases, high CO and water concentrations during FT synthesis inhibited secondary reactions of hydrocarbons. The reaction schemes in CO_2 hydrogenation are generally consistent with the phenomena observed in CO hydrogenation [13]. The overall reaction scheme may be shown in Scheme 1.

We have investigated the effect of the interaction between metal and reactants on the distribution of products from CO_2 hydrogenation on iron catalyst with ruthenium added. Particularly, we examine the CO_2 conversion and hydrocarbon distribution through the adsorption abilities of CO_2, CO, H_2 and C_2H_4. Detailed analyses of waxy product were also conducted. Finally, the effect of ruthenium added to iron catalyst by impregnation was carefully studied particularly with respect to waxy products.

Scheme 1. The overall reaction in CO_2 hydrogenation [13].
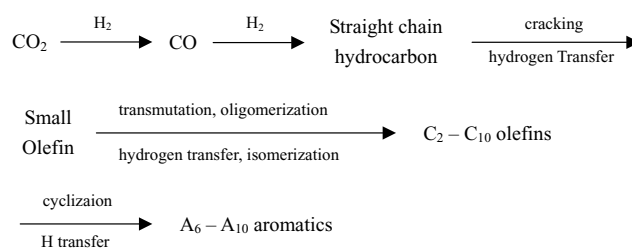
2. Experimental

Fe-K/γ-Al_2O_3 and Fe-Ru-K/γ-Al_2O_3 catalysts are prepared by the impregnation of γ-Al_2O_3 with aqueous solutions of $Fe(NO_3)_3\cdot9H_2O$ and K_2CO_3 with or without $RuCl_3$. The nominal catalyst compositions were 1.00 Fe/0.35 K/5.00 Al_2O_3 and 1.00 Fe/0.05 Ru/0.35 K/5.00 Al_2O_3. The impregnated catalysts were homogeneously mixed, and a small amount of water was added. Pellets of 3 mm in length were extruded through a 1.5 mm diameter die. These pellets were dried at 393 K for 12 h and calcined at 773 K for 24 h in air.

CO_2 hydrogenation was carried out in a bench scale fixed bed reactor (1.6 cm i.d. × 60 cm high). A schematic diagram of the fixed bed reactor system used is shown in Fig. 1. The reaction and internal standard gases (CO_2, H_2, N_2 and He)
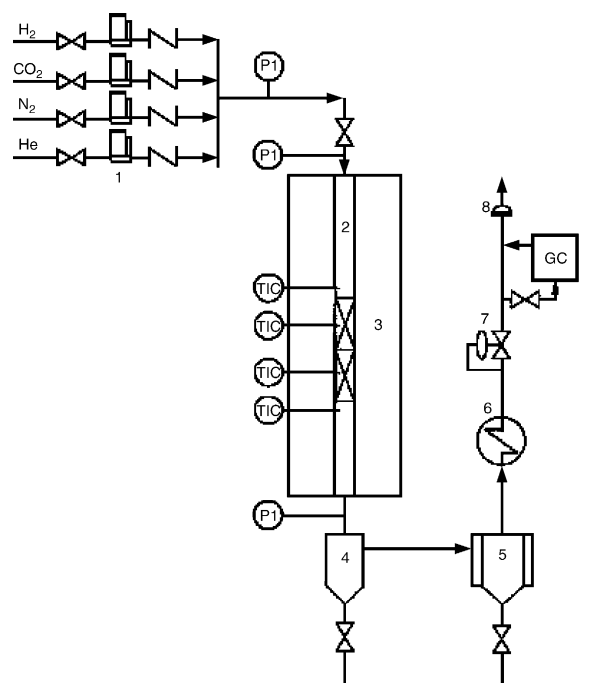
1. Mass flow controller	5. Condenser
2. Fixed bed reactor	6. Heat exchanger
3. Electric heater	7. Back pressure regulator
4. Gas-liquid separator	8. Digital flow meter

Fig. 1. Experimental apparatus.

were taken from cylinders and their flow rates were controlled by MFC (mass flow controller, Brooks Co.). Reaction temperature was controlled at 573 K and reaction pressure was maintained at 10 atm by back pressure regulator (BPR, Tescom Co.). 21.0 g of catalysts were filled up and the flow rate of the mixed gas was 2000 ml/g-cat h at STP. The composition of the gas was $H_2/CO_2 = 3/1$. The liquid products were separated from gas products in the gas–liquid separator and condenser. The exit gas flow rate was measured by a digital bubble flow meter to evaluate the reaction conversion. The gaseous products were analyzed by two kinds of on-line GC–TCD using internal standard gases, N_2 and He, to check the consumption of CO_2 and H_2, respectively. With the data obtained from the GC–TCD analysis, the conversion of CO_2 and the yield of CO and CH_4 were calculated. The peak areas of organic products were referred to the peak areas of CH_4 (GC–TCD); the organic product selectivity and yields were determined from the GC–FID analysis.

Temperature-programmed desorption (TPD) measurement was carried out on a conventional TPD system equipped with a TCD cell. In order to remove water and impurities on surface, the H_2-reduced catalysts was exposed to He gas at 823 K for 4 h. After this pretreatment, the samples were exposed to ammonia, carbon dioxide, ethane or carbon monoxide for 1 h. Finally, the programmed heating at a rate of 10 K/min was started and then followed by heating to 823 K. The amount of the desorbed gas was continuously monitored by TCD. In the pulse chemisorption, the peak area corresponding to a pulse of hydrogen in helium gas passed over a catalyst sample is measured before and after contact with the catalyst.

X-ray powder diffraction was used to examine the crystallinity of the catalysts. Diffraction patterns were collected at $10°$ min^{-1} on a Rigaku 2155D6 X-ray diffract meter with a Cu Kα X-ray source. The BET surface area and pore size distribution (PSD) were measured using Micrometrics ASAP 2000. All catalyst were degassed before the measurement. The degassing was carried out under vacuum at 393 K for 3 h and then 573 K for 5 h.

3. Results and discussion

3.1. Characterization of iron-based catalysts

The composition of iron-based catalysts is summarized in Table 1 and the pore volume is shown in Fig. 2. The BET
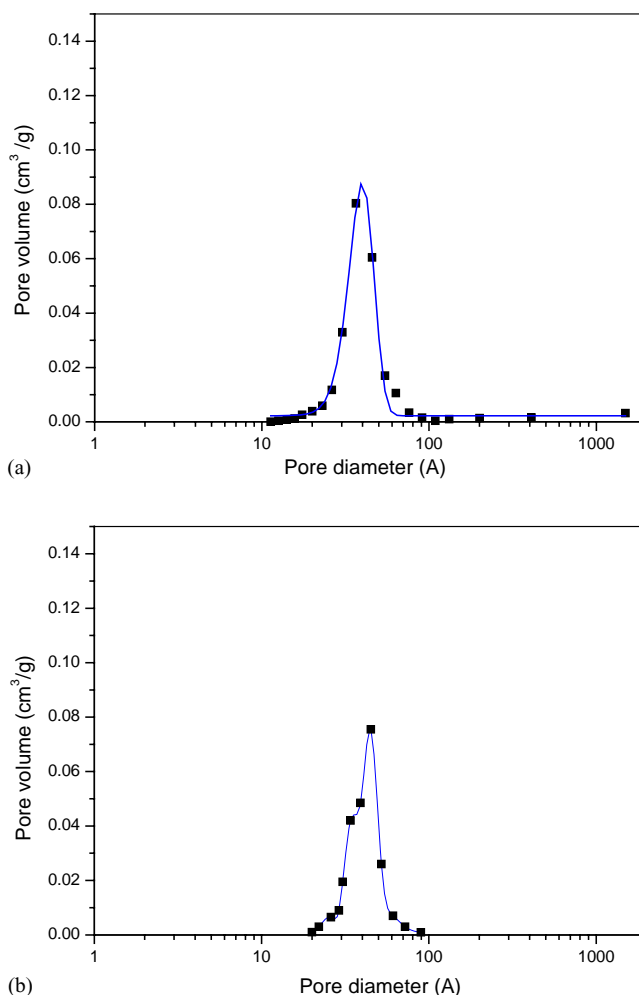

Fig. 2. Pore size distribution of iron-based catalysts. (a) Fe-Ru-K/γ-Al$_2$O$_3$, (b) Fe-K/γ-Al$_2$O$_3$.

surface area and pore volume obtained for Fe-K/γ-Al$_2$O$_3$ catalyst were 133 m^2/g and 0.36 ml/g, respectively. The physical properties of Fe-Ru-K/γ-Al$_2$O$_3$ catalyst were similar to those of Fe-K/γ-Al$_2$O$_3$ catalyst. The pore size distribution of Fe-Ru-K/γ-Al$_2$O$_3$ catalyst was unchanged in spite of the addition of Ru component.

Fig. 3 shows X-ray diffractions of the catalysts. After calcination under air condition, iron components assigned to FeO (49.8°), Fe$_2$O$_3$ (33.4°), Fe$_3$O$_4$ (35.9°), and α-Fe (64.4°) were observed. However, XRD peaks for ruthenium component ($2\theta = 44.0, 28.5°$) were absent for both catalysts. The dispersion of ruthenium components on the freshly

Table 1
Physical properties of the Fe-K/γ-Al$_2$O$_3$ and Fe-Ru-K/γ-Al$_2$O$_3$

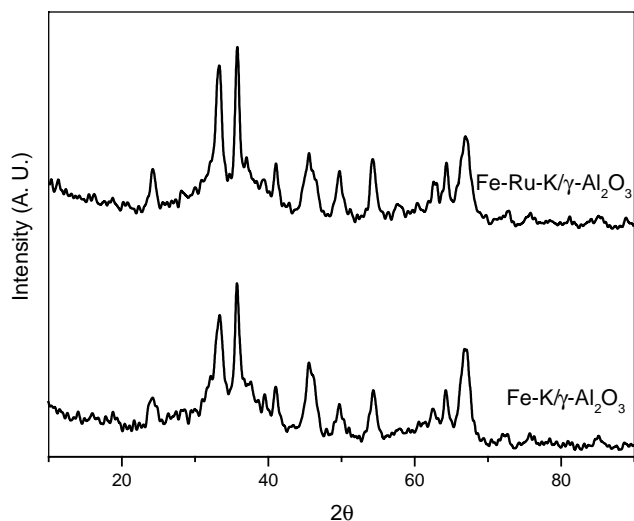|	BET surface area (m^2/g)	Mean pore diameter (Å)	Pore volume (cc/g)	Fe loading[a] (wt.%)	Ru loading[a] (μmol/g)	H$_2$ uptakes (μmol/g)	Ru dispersion (%)
Fe-K/γ-Al$_2$O$_3$	133	44	0.36	19.1	–	27.4	69.8
Fe-Ru-K/γ-Al$_2$O$_3$	132	41	0.33	19.8	1.3	1.9	–

[a] ICP analysis.

Fig. 3. XRD profiles of iron-based catalysts.

reduced catalysts is determined by H_2 pulse chemisorption at 373 K. The results are shown in Table 1 as well. Moss et al. pointed out that H_2 chemisorption at 373 K was reliable for determining the amount of active surface metal on ruthenium catalysts [18,19]. From Table 1, it is seen that H_2 uptakes on the Fe-Ru-K/γ-Al_2O_3 catalyst is obviously higher than those on the Fe-K/γ-Al_2O_3 catalyst. Table 1 also shows the ruthenium dispersions of the Fe-Ru-K/γ-Al_2O_3 catalyst calculated on the basis of the H_2 uptakes. The ruthenium dispersion of this catalyst is high at 70%. In the XRD pattern and H_2 pulse chemisorption shown that the ruthenium component is highly dispersed on the Fe-based catalyst.

Fig. 4 shows the results indicating the influence of ruthenium component on the acidity of the catalysts. The NH_3-TPD method was considered to be an effective characterization technique for the determination of total surface acidity [21]. In general, three ammonia desorption peaks at approximately 400, 550 and 800 K were reported [22,23] for
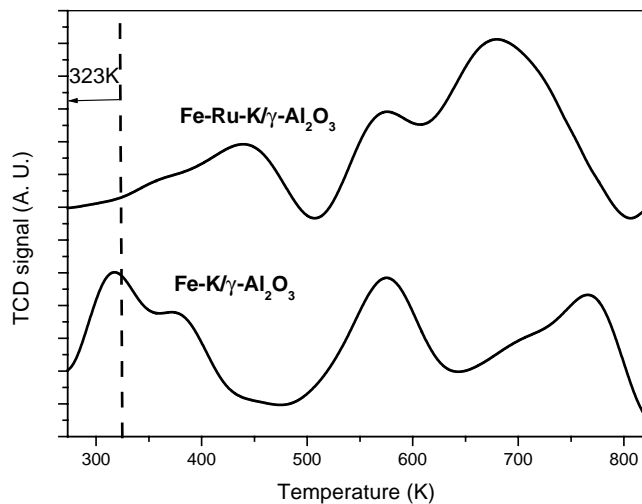
iron-based catalyst. These three desorptions were regarded as the weakly held ammonia, i.e., ammonia adsorbed on weak acid sites or hydrogen-bonded sites which related to the aluminum species, the medium chemisorbed ammonia on the medium acid sites which related to the iron–aluminum species, and the strongly chemisorbed ammonia or ammonium cations on the strong acid sites which related to the iron species, respectively. Fe-K/γ-Al_2O_3 without a ruthenium component exhibited three main peaks at approximately 400, 550 and 750 K. On the other hand, in the TPD profile pattern of Fe-Ru-K/γ-Al_2O_3, the low-temperature desorption peak was shifted to 450 K, the medium-temperature desorption was 570 K, and the high-temperature desorption peak was increased in intensity and shifted to the low temperature range. Therefore, on the ruthenium-added catalyst, the amount of strong acid site was increased and the strength of weak acid site was increased.

3.2. CO_2 hydrogenation in iron-based catalytic systems

The catalytic activities of Fe-K/γ-Al_2O_3 and Fe-Ru-K/γ-Al_2O_3 are compared in Fig. 5. Initially, the activities slowly increased until they leveled off. Then they had a steady state. When Fe-K/γ-Al_2O_3 was used, the conversion of CO_2 was 36%, while in the case of Fe-Ru-K/γ-Al_2O_3 the conversion of CO_2 was 41%. CO_2 conversion was high in the presence of Ru compared with Fe-K/γ-Al_2O_3. This result showed that the number of active sites on Fe-K/γ-Al_2O_3 was increased by addition of the ruthenium component. It has been reported that the resulting larger number of nuclei then led to a better dispersion of the reduced phases and to a larger number of active sites for the Fischer–Tropsch synthesis [20]. As shown in Fig. 3 and Table 1, the ruthenium peaks were not shown due to high dispersion on Fe-Ru-K/γ-Al_2O_3. From these data, it is confirmed that the high CO_2 conversion on
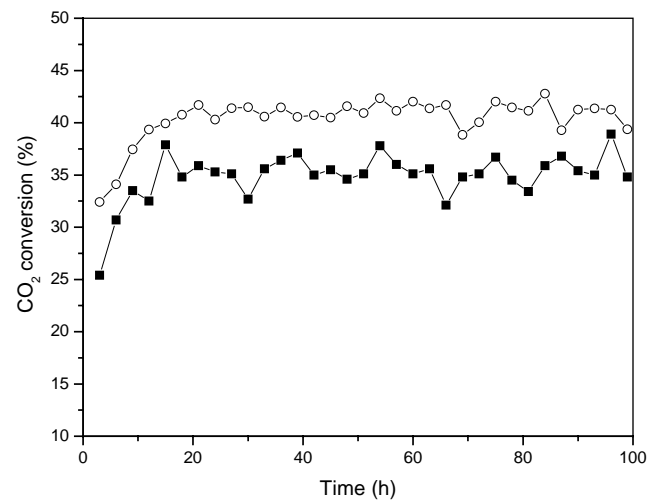

Fig. 5. Catalytic activity of CO_2 hydrogenation. Reaction conditions: $T = 573$ K, $P = 10$ atm, S.V. = 2000 ml/g-cat h, $H_2/CO_2 = 3$ Fe-Ru-K/γ-Al_2O_3 (○), Fe-K/γ-Al_2O_3 (■).
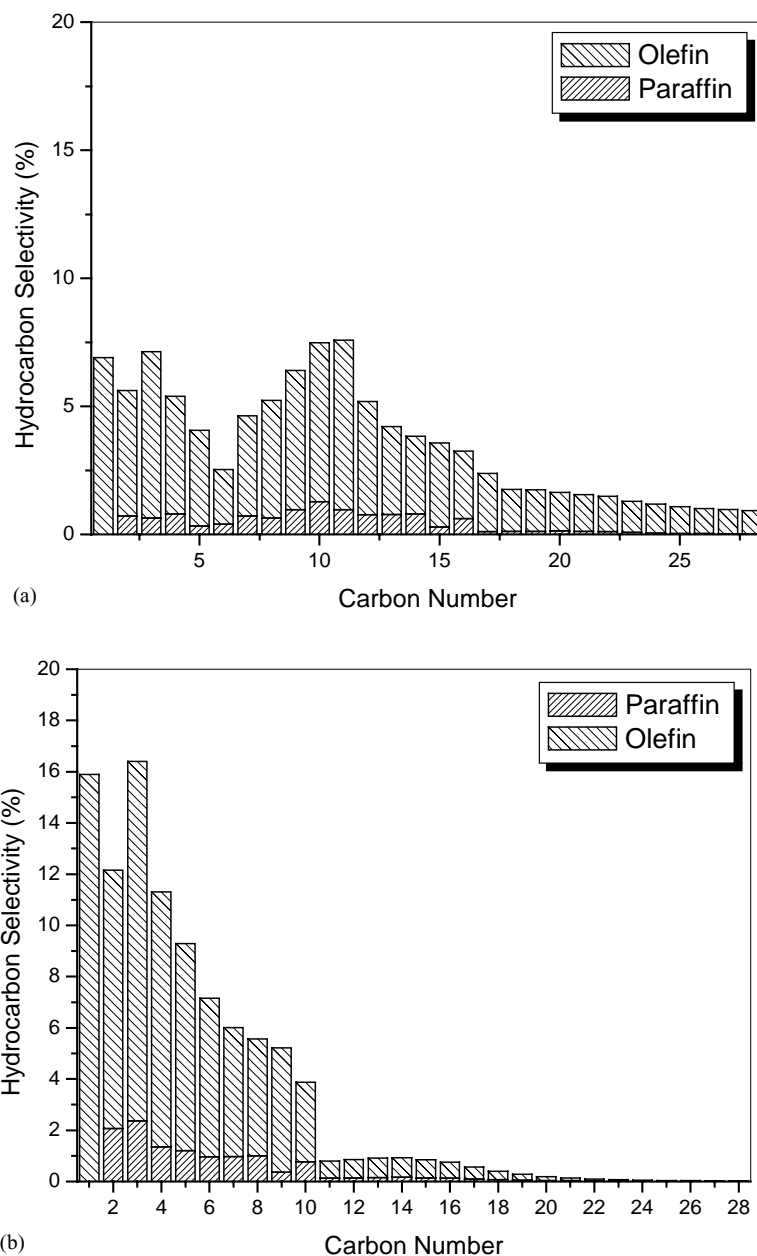

Fig. 4. NH_3-TPD profiles of iron-based catalysts.

Fig. 6. Olefin distribution in hydrocarbon products of CO_2 hydrogenation in iron-based catalysts. (a) Fe-Ru-K/γ-Al$_2$O$_3$, (b) Fe-K/γ-Al$_2$O$_3$.

ruthenium promoted catalyst relates to high dispersion of the ruthenium component.

Fig. 6 presents the product distribution in CO_2 hydrogenation over these catalysts. Fe-K/γ-Al$_2$O$_3$ catalyst showed higher selectivities for methane (16 C mol%) and C_2–C_4 hydrocarbons (39.6 C mol%) compared with Fe-Ru-K/γ-Al$_2$O$_3$. For Fe-Ru-K/γ-Al$_2$O$_3$, the amount of lighter hydrocarbons was small, but that of higher hydrocarbons increased. The main products over Fe-K/γ-Al$_2$O$_3$ were lighter hydrocarbons such as C_1–C_4 hydrocarbons, and those over Fe-Ru-K/γ-Al$_2$O$_3$ were higher hydrocarbons such as C_5–C_{15} hydrocarbons. In the case of Fe-K/γ-Al$_2$O$_3$, the product distribution follows the ASF

distribution. In fact, the ASF distribution is based on the mechanism consisting of three independent steps, which can be described by Eqs. (1)–(3). The mechanism includes the initial step and propagation steps. However, in the case of Fe-Ru-K/γ-Al$_2$O$_3$ catalytic system, hydrocarbon distribution deviates from the ideal ASF distribution. In general, this deviation is caused by secondary reaction of the primary hydrocarbon products, such as reinsertion into the chain growth process, hydrogenation, and hydrogenolysis [16,17]. It was previously shown that the rates of reinsertion and hydrogenation increase exponentially with chain length. Therefore, the behavior of catalysts with and without ruthenium will be explained using the CO_2-, CO-, and
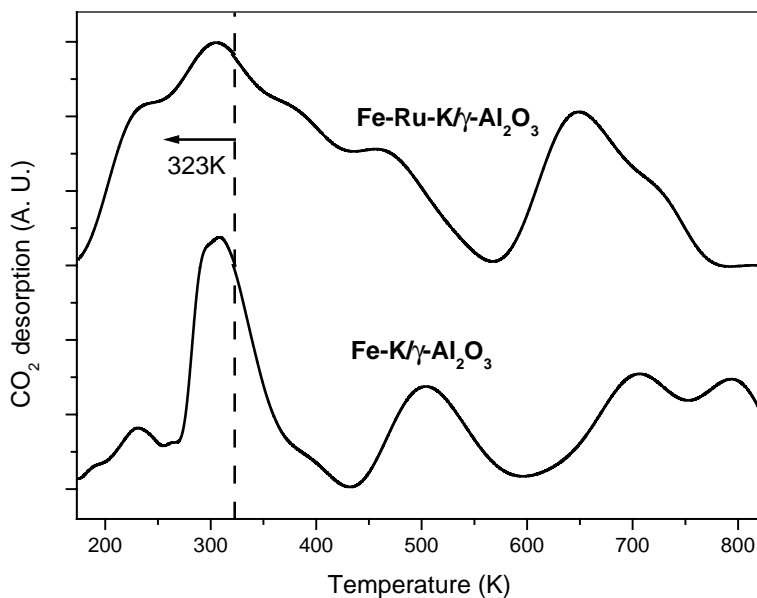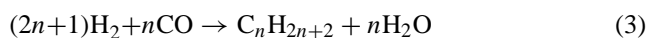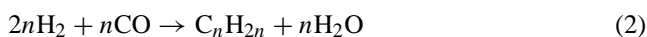
Fig. 7. CO_2-TPD profiles of iron-based catalysts.

C_2H_4-TPD experiments.

$$CO_2 + H_2 \rightarrow CO + H_2O \qquad (1)$$

$$2nH_2 + nCO \rightarrow C_nH_{2n} + nH_2O \qquad (2)$$

$$(2n+1)H_2 + nCO \rightarrow C_nH_{2n+2} + nH_2O \qquad (3)$$

The TPD spectra obtained after CO_2 adsorption on Fe-K/γ-Al_2O_3 and Fe-Ru-K/γ-Al_2O_3 are shown in Fig. 7. The amount of desorbed CO_2 and the temperature of maximum desorption of CO_2 are the criteria for the amount and strength of basic sites, respectively [25]. Two desorption peaks were observed around 500 and 670 K for the catalysts with and without the ruthenium component, respectively. It is reasonable to assign the peak at a lower temperature to a bicarbonate species resulting from the interaction of CO_2 with basic hydroxyl groups of catalysts. The peak at higher temperature could be attributed to a carbonate species, which exhibited a higher thermal stability than hydrogen carbonate species [26]. In the case of Fe-Ru-K/γ-Al_2O_3, the strength of basicity was decreased. On the other hand, it was revealed by TPD that the total amount of adsorbed CO_2 was larger for Ru-added catalyst than for Fe-K/γ-Al_2O_3. The CO_2 adsorption amount for Fe-Ru-K/γ-Al_2O_3 was 664 μmol/g, while for Fe-K/γ-Al_2O_3 it was 514 μmol/g This result indicates that, when ruthenium component was added, the adsorption amount of CO_2 on the basic sites was increased and the adsorption strength was decreased. It is considered that the increase in CO_2 conversion for Fe-Ru-K/γ-Al_2O_3 is due to the increase in CO_2 adsorption amount.

Fig. 8 illustrates the TPD profiles for carbon monoxide after adsorption at 293 K. The TPD profile consisted of four bands, with maximum at about 400, 480, 530, and 840 K. Three desorption peaks around T_m = 400 and 480, and 530 K were found to correspond to CO desorption, while

that at the higher temperature was caused by the simultaneous desorption of CO, CO_2, and a small amount of CH_4 [27]. This means that the physically adsorbed CO resulted in no decomposition. The desorption of CO and CO_2 above 550 K is due to CO desorption adsorbed chemically. According to Rathousky [28], the most strongly bonded forms of CO adsorbed on the catalyst surface were bridge forms, which were apparently responsible for the occurrence of dissociative CO adsorption. Our result supports the claim [24] that a substantial heat of adsorption (>50 kJ/mol) was responsible for the peak in the TPD profile in the temperature region above 573 K. The desorption peak was also observed at 800 K on Fe-K/γ-Al_2O_3. However, in the case of ruthenium promoted catalyst, the desorption peak was observed at 840 K. This result suggests that the bonding strength between CO and active sites on the ruthenium-added catalyst is greater than that without a ruthenium. The strength between active species and CO could be related to CO selectivity in CO_2 hydrogenation. Therefore, the probability of hydrocarbon propagation was high because of strong bonding between CO and active sites over Fe-Ru-K/γ-Al_2O_3; as a result, CO selectivity in CO_2 hydrogenation decreased.

In addition, the result shown in Fig. 8 could be explained by the principle of activation energy. The activation energies of CO adsorption were measured through CO-TPD experiment with various rates of heating temperature. Ozawa et al. presented an equation to calculate the activation energy based on the shift of the maximum deflection temperature (T_m) upon changing the heating rate [29,30].

$$\log \phi + 0.456 \frac{E_a}{RT_m} = \text{constant}$$

In this equation, ϕ is the heating rate (K/min), T_m the maximum deflection temperature (K), E_a the activation
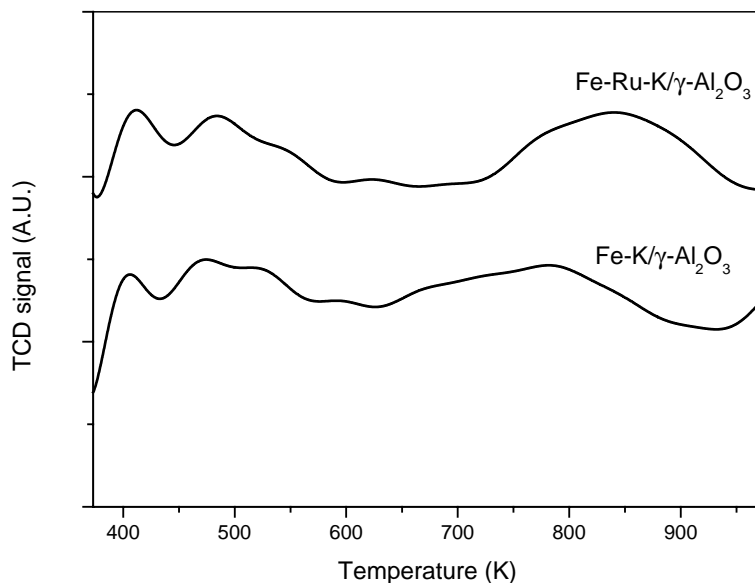
Fig. 8. CO-TPD profiles of iron-based catalysts.

energy, and R the gas constant. The activation energy could be derived from the slope of linear plot of $\log \phi$ versus $1/T_m$.

The calculated activation energy of CO adsorption are presented in Table 2. At the maximum temperature,

Table 2
The activation energy for CO adsorption (at maximum temperature (T_m)) on the Fe-K/γ-Al$_2$O$_3$ and Fe-Ru-K/γ-Al$_2$O$_3$

Catalysts	Heating rate (ϕ)			Activation energy (E_a, kcal/mol)
	5 K/min	10 K/min	15 K/min	
Fe-K/γ-Al$_2$O$_3$	755	803	890	10.13
Fe-Ru-K/γ-Al$_2$O$_3$	818	839	920	13.04

the activation energies obtained for desorption of CO on Fe-K/γ-Al$_2$O$_3$ and Fe-Ru-K/γ-Al$_2$O$_3$ were 10.1 and 13.0 kcal/mol, respectively. Consequently, the activation energy of the catalyst with ruthenium component was stronger than that without ruthenium. As the interaction of active species and CO is strong, it is expected that the probability of chain growth is increased.

Fig. 9 shows the TPD profiles of ethene after adsorption at 293 K. Linear α-olefins are known to be the main primary organic products of FT synthesis. Once formed they can readsorb on the catalyst surface and undergo secondary reactions: hydrogenation, isomerization, re-insertion, hydrogenolysis and hydroformylation (Scheme 2). Paraffins
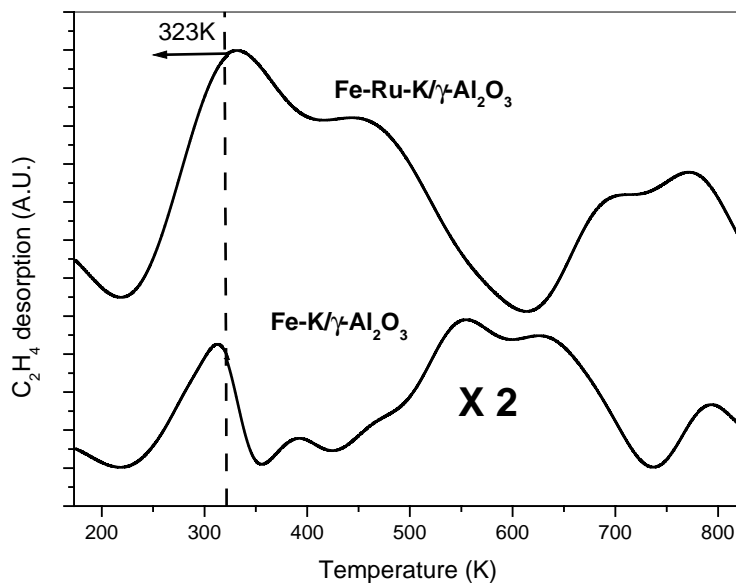
Fig. 9. C$_2$H$_4$-TPD profiles of iron-based catalysts.
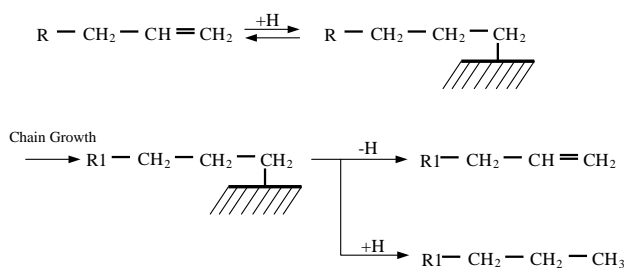
Scheme 2. Readsorption mechanism in CO_2 hydrogenation.

are believed to be one of products of CO_2 hydrogenation, formed by associative desorption of an alkyl- and a H-surface species: Alternatively α-olefins are formed via dissociative desorption. However, they can readsorb and form an alkyl chain attached to the catalyst surface. This surface species can again either grow further or desorb as an olefin or a paraffin, the latter reaction thereby leading to hydrogenation of the readsorbed olefin [16,17,31]. Therefore, the readsorption of α-olefin products played a critical role in hydrocarbon chain growth. The nature of hydrocarbon adsorbed, which was formed during the reaction, was investigated through C_2H_4-TPD experiments. The C_2H_4-TPD profile consisted of one peak below 300 K and three peaks ranging from 500 to 700 K. A peak at low temperature was regarded as the weakly held ethene. On the other hand, the peak at high temperature was caused by the strongly bonded forms of C_2H_4 adsorbed on the catalyst surface. Desorption temperature in C_2H_4-TPD reflected the adsorption strength between catalytic surface and ethene. The C_2H_4 desorption temperature on Fe-Ru-K/γ-Al_2O_3 was higher than that on Fe-K/γ-Al_2O_3. This indicates that the C_2H_4 adsorption strength on Fe-Ru-K/γ-Al_2O_3 was stronger than that on Fe-K/γ-Al_2O_3. In the case of Fe-Ru-K/γ-Al_2O_3, the produced α-olefin is easily adsorbed on catalyst surface, and

then undergoes the secondary propagation. Therefore, the chain length of hydrocarbon is increased.

3.3. Characteristics and analysis of the microcrystalline wax

In this study, we could obtain the wax product after CO_2 hydrogenation, although there are very few reports on the synthesis and analysis of the waxy product in CO_2 hydrogenation.

The crystal phase of the wax, which was produced by the Fe-Ru-K/γ-Al_2O_3 catalytic system, was examined using powder X-ray diffraction (XRD) as shown in Fig. 10. The peak at 21.5° was assigned to (1 0 0) plane reflection and that at 23.9° to (2 0 0) plane reflection of produced wax. Crystallite size was calculated along the (1 1 0) and (2 0 0) plane directions using the Scherrer formula. The crystalline size in the (1 1 0) plane direction was 36.7 nm, while that in the (2 0 0) plane direction was 30.6 nm. The crystallite size of wax was larger than that of commercial wax (about 20 nm).

To better understand the emergence of crystalline morphology in microcrystalline wax, a polarizing optical microscope was used. Fig. 11 shows polarized optical micrographs of wax after cooled from 423 to 298 K. At 423 K, microcrystalline wax was completely molten. With a decrease in temperature, the nematic textures displayed strong birefringence resembling schlieren textures. From these results, it was concluded that the wax, which was produced in Fe-Ru-K/γ-Al_2O_3 catalytic system, had high crystallinity.

The microcrystalline wax was identified by NMR. The ^{1}H NMR and ^{13}C NMR patterns of microcrystalline wax are shown in Fig. 12(a) and (b), respectively. For the ^{1}H NMR pattern, the peak at 1.0 ppm was assigned to the terminal methyl protons adjacent to carbon atoms in the main chain backbone. The singlet at 1.2 ppm was attributed to the
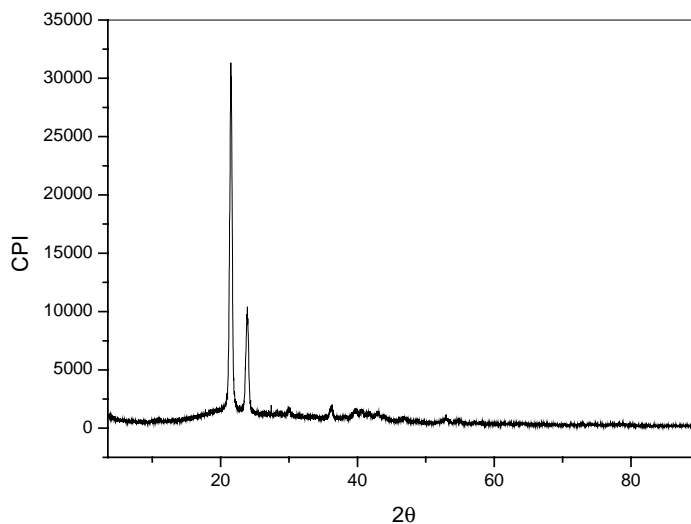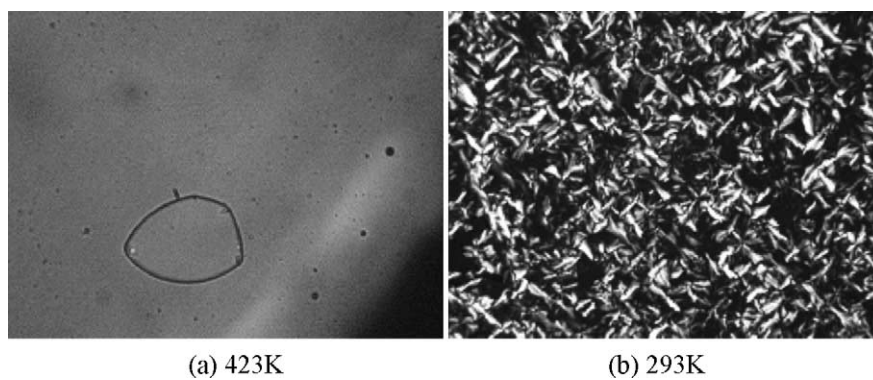

Fig. 10. XRD profile of wax product in Fe-Ru-K/γ-Al_2O_3.

(a) 423K   (b) 293K

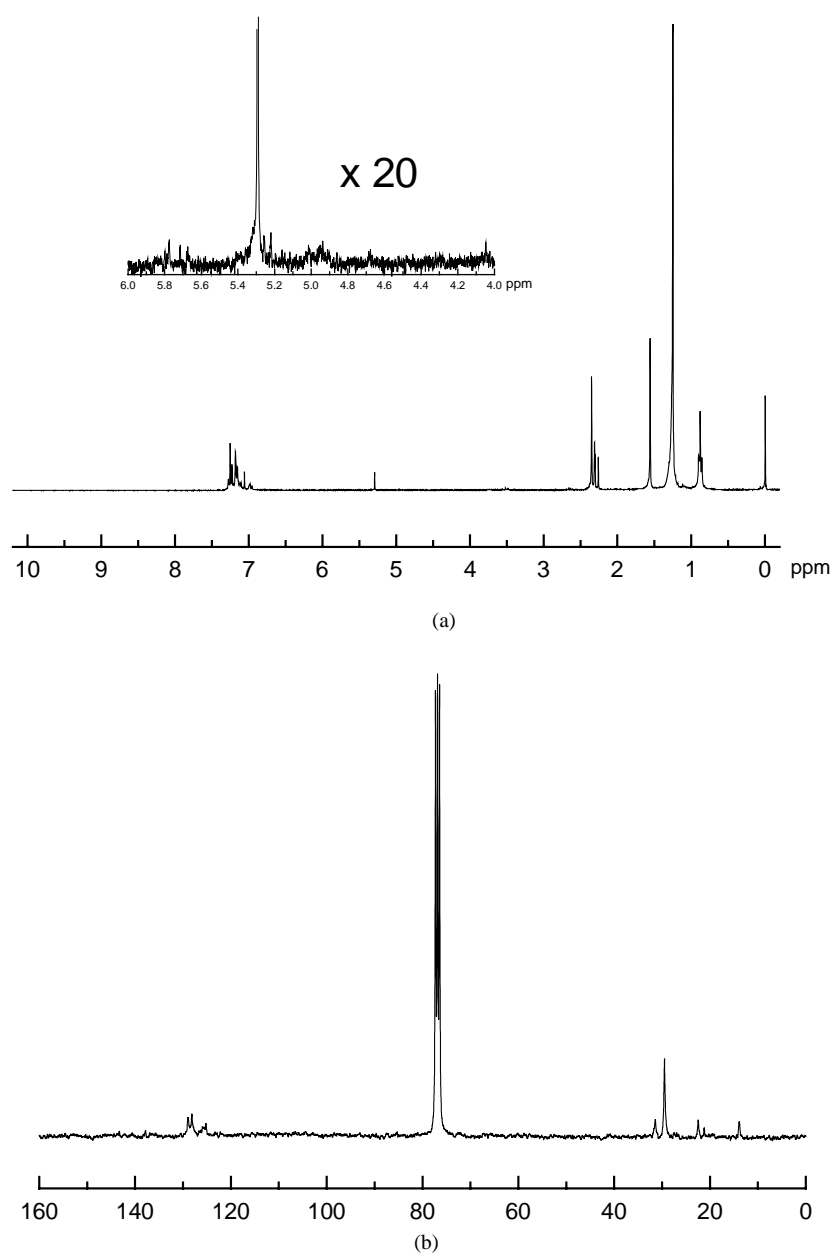Fig. 11. The polarized optical micrographs of wax product after cooling from 423 to 298 K.

(a)

(b)

Fig. 12. NMR profile of wax product in Fe-Ru-K/γ-Al$_2$O$_3$. (a) ^{1}H NMR, (b) ^{13}C NMR.

Table 3
GPC analysis of wax product on the Fe-K/γ-Al$_2$O$_3$ and Fe-Ru-K/γ-Al$_2$O$_3$

Sample	M_n	M_w	M_w/M_n
Fe-K/γ-Al$_2$O$_3$	80	380	4.75
Fe-Ru-K/γ-Al$_2$O$_3$	1280	2870	2.24

resonance of –CH$_2$– in the main chain. The signals at 1.6 and 2.3 ppm were due to methylene, which was adjacent to the internal olefin in the main chain. The peaks at 5.5 ppm were due to olefinic function, which was the olefinic group at the chain end. The multiplet at 7.0 ppm originated from the aromatic group [32]. The ^{13}C NMR spectra of microcrystalline wax are shown in Fig. 12(b). The peak centered at 14 ppm was mainly due to the carbon resonance for the terminal CH$_3$ group in the main chain. The resonance between 15 and 27 ppm was due to the branched alkane CH$_3$ group. The peaks at 29 and 31 ppm were associated with the internal methylene carbon in the main chain of wax. The olefinic group appeared in the region of 125–130 ppm. From these NMR spectra, the microcrystalline wax, which was produced in the Fe-Ru-K/γ-Al$_2$O$_3$ catalytic system, was confirmed to have more olefin fraction than the generally obtained FT wax. Particularly, the wax products have the olefinic function at the chain end. The olefinic group at the chain end could be applied to functionalization.

Table 3 and Fig. 13 present the gel permeation chromatography (GPC) analysis results of the wax produced in the iron catalytic systems. The hydrocarbon produced over Fe-K/γ-Al$_2$O$_3$ showed the number average molecular weight (M_n) of 80 and the weight average molecular weight (M_w) of 380. When the Ru component was added, the microcrystalline wax with the M_n of 1280 and the M_w of 2870 was obtained. These values were dramatically high compared with the wax produced without a ruthenium.
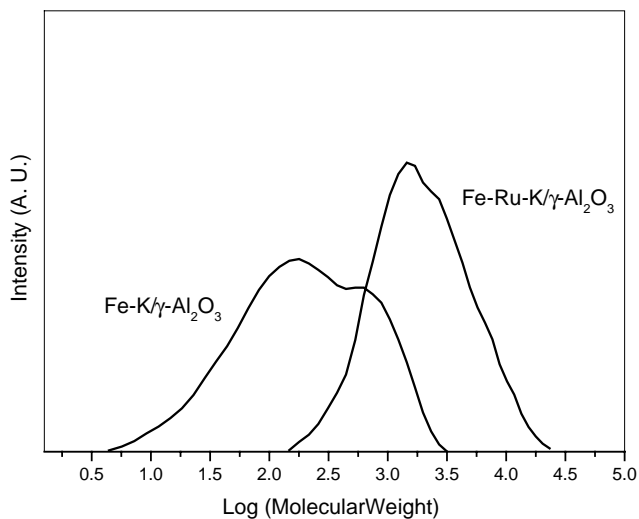
In this study, it was confirmed that ruthenium component promoted the readsorption ability of α-olefin, increasing the chain length of hydrocarbon. In addition, the microcrystalline wax produced in CO$_2$ hydrogenation was highly crystalline and olefin-rich hydrocarbon. Particularly, the wax products have the olefinic functions at the chain end. Upon addition of ruthenium component, the carbon chain length of microcrystalline wax became longer. Therefore, it is expected that the produced solid hydrocarbon could be applied to the macromonomer.

4. Conclusion

The main results of this study are as follows.

1. The probability of α-olefin readsorption in CO$_2$ hydrogenation increased by the ruthenium component. As a result, higher hydrocarbons could be easily produced in the Fe-Ru-K/γ-Al$_2$O$_3$ catalytic system, and hydrocarbon distribution deviated from the ideal ASF distribution. High yield of solid hydrocarbon was obtained from carbon dioxide and hydrogen on Fe-Ru-K/γ-Al$_2$O$_3$.
2. The microcrystalline wax produced in CO$_2$ hydrogenation was high-crystalline and olefin-rich hydrocarbon. Its chain length was longer when ruthenium component was added to the iron-based catalyst. Therefore, it is expected that the produced solid hydrocarbon could be applied to the macromonomer.

Fig. 13. GPC profile of waxy product in iron-based catalysts.

References

[1] J. Nerlov, S. Sckerl, J. Wambach, I. Chorkendorff, Appl. Catal. A 191 (2000) 97.
[2] T. Inui, H. Hara, T. Takeguchi, K. Ichino, J. Kim, S. Iwamoto, S. Pu, Energy Conv. Manage. 38 (1997) 385.
[3] M. Choi, J. Kim, H. Kim, Y. Kang, S. Lee, K. Lee, Korean J. Chem. Eng. 18 (2001) 646.
[4] J. Hwang, E. Seo, S. Choung, Hwahak Konghak 38 (2000) 767.
[5] M. Stocker, Microporous Mesoporous Mater. 29 (1999) 3.
[6] Y. Tan, M. Fujiwara, H. Ando, Q. Xu, Y. Souma, Ind. Eng. Chem. Res. 38 (1999) 3225.
[7] M. Aresta, I. Tommasi, Energy Conv. Manage. 38 (1997) s373.
[8] M. Aresta, M. Galatola, J. Cleaner Prod. 7 (1999) 181.
[9] S. Fang, K. Fujimoto, Appl. Catal A 142 (1996) L1.
[10] T. Zhao, Y. Han, Y. Sun, Fuel Process. Technol. 62 (2000) 187.
[11] N. Tsubaki, K. Fujimoto, Fuel Process. Technol. 62 (2000) 173.
[12] A. Trovarelli, C. Mustazza, G. Dolcetti, Appl. Catal. 65 (1990) 129.
[13] C. Kuei, M. Lee, Can. J. Chem. Eng. 69 (1991) 347.
[14] M.J.L. Gines, A.J. Marchi, C.R. Apesteguia, Appl. Catal. A 154 (1997) 155.
[15] J. Patzlaff, Y. Liu, C. Graffmann, J. Gaube, Appl. Catal. A 186 (1999) 109.
[16] E. Iglesia, S.C. Reyes, R.J. Madon, J. Catal. 129 (1991) 238.
[17] E. Iglesia, S.C. Reyes, R.J. Madon, S.L. Soled, Adv. Catal. 39 (1993) 221.
[18] R.L. Moss, in: R.B. Anderson, P.T. Dawson (Eds.), Experimental Methods in Catalytic Research, vol. 2, Academic press, New York, 1976, p. 70.

[19] V.A. Mazzieri, P.C. L'Argentiëre, F. Coloma-Pascual, N.S. Figoli, Ind. Eng. Chem. Res. 42 (2003) 2269.

[20] S. Li, S. Krishnamoorthy, A. Li, G.D. Meitzner, E. Iglesia, J. Catal. 206 (2002) 202.

[21] S. Hong, G. Seo, Y. Uh, Korean J. Chem. Eng. 15 (1998) 566.

[22] J.A. Martens, W. Souverijns, W.V. Rhijn, P.A. Jacobs, in: G. Ertl, H. Knözinger, J. Weitkamp (Eds.), Handbook of Heterogeneous Catalysis, vol. 1, VCH, Weinheim, 1997, p. 327.

[23] L. Yang, Y. Aizhen, X. Qinhua, Appl. Catal. 67 (1997) 169.

[24] J.C. Lavelley, Catal. Today 27 (1996) 377.

[25] K. Arishtrirova, P. Kovacheva, A. Predoeva, Appl. Catal. A 243 (2003) 191.

[26] A.C. Phukan, R.K. Boruah, Sep. Purif. Technol. 17 (1999) 189.

[27] N. Katada, T. Miyamoto, H.A. Begum, N. Naito, M. Niwa, A. Matsumoto, K. Tsutsumi, J. Phys. Chem. B 104 (2000) 5511.

[28] A. Lapidus, A. Krylova, J. Rathousky, A. Zukal, M. Jancalkova, J. Mol. Catal. 71 (1992) 183.

[29] T. Ozawa, J. Therm. Anal. 5 (1973) 563.

[30] M. Kang, J. Mol. Catal. A 3856 (2002) 1.

[31] H. Schulz, M. Claeys, Appl. Catal. A 186 (1999) 71.

[32] K. Endo, K. Senoo, Y. Takakura, Eur. Polym. J. 35 (1999) 1413.